Thickness-self-controlled synthesis of porous transparent polyaniline-reduced graphene oxide composites towards advanced bifacial dye-sensitized solar cells

CrossMark

Yu-Sheng Wang [a], Shin-Ming Li [a], Sheng-Tsung Hsiao [a], Wei-HaoLiao [a], Shin-Yi Yang [a,b], Hsi-Wen Tien [a,b], Chen-Chi M. Ma [a,**], Chi-Chang Hu [a,*]
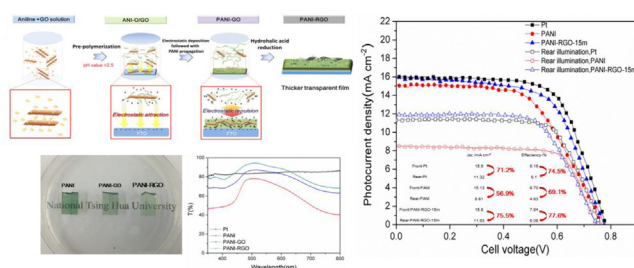
[a] Department of Chemical Engineering, National Tsing-Hua University, Hsin-Chu 30013, Taiwan, ROC
[b] Exp Interconnect Division, Taiwan Semiconductor Manufacturing Company, Ltd., 168, Park Ave. 2, Hsin-Chu Science Park, Hsin-Chu 30075, Taiwan, ROC

HIGHLIGHTS

- A two-step approach is demonstrated to fabricate a porous, ultrathin PANI-RGO electrode.
- The thickness can be self-controlled by pH adjustment.
- The well-designed PANI-RGO electrodes exhibit excellent photovoltaic performances.
- The incorporation of RGO raises the transparency of PANI and photo harvest.
- A universal approach is well-designed to fabricate PANI-RGO-based conductive thin films.

GRAPHICAL ABSTRACT

ABSTRACT

A powerful synthesis strategy is proposed for fabricating porous polyaniline-reduced graphene oxide (PANI-RGO) composites with transparency up to 80% and thickness from 300 to 1000 nm for the counter electrode (CE) of bifacial dye-sensitizing solar cells (DSSCs). The first step is to combine the *in-situ* positive charge transformation of graphene oxide (GO) through aniline (ANI) prepolymerization and the electrostatic adsorption of ANI oligomer-GO to effectively control the thickness of ultrathin PANI-GO films by adjusting pH of the polymerization media. In the second step, PANI-GO films are reduced with hydroiodic acid to simultaneously enhance the apparent redox activity for the I_3^-/I^- couple and their electronic conductivity. Incorporating the RGO increases the transparency of PANI and facilitates the light-harvesting from the rear side. A DSSC assembled with such a transparent PANI-RGO CE exhibits an excellent efficiency of 7.84%, comparable to 8.19% for a semi-transparent Pt-based DSSC. The high light-harvesting ability of PANI-RGO enhances the efficiency retention between rear- and front-illumination modes to 76.7%, compared with 69.1% for a PANI-based DSSC. The higher retention reduces the power-to-weight ratio and the total cost of bifacial DSSCs, which is also promising in other applications, such as windows, power generators, and panel screens.

© 2014 Elsevier B.V. All rights reserved.

 * Corresponding author. Tel.: +886 3 5719036; fax: +886 3 5715408.
 ** Corresponding author. Tel.: +886 3 5713058; fax: +886 3 5715408.
   E-mail addresses: ccma@che.nthu.edu.tw (C.-C.M. Ma), cchu@che.nthu.edu.tw (C.-C. Hu).

1. Introduction

Bifacial dye-sensitising solar cells (DSSCs) have recently attracted the attention of several research groups [1–5] because of a higher light-harvesting efficiency regarding the ability of both-side incident illumination absorption. This property substantially reduces the cost of energy generation and the limitation of the incident angle and direction of DSSCs. Moreover, the transparent property renders the bifacial DSSCs a highly promising device for building-integrated photovoltaic systems and portable power generators in which the bifacial DSSCs must combine with transparent substrates, such as building windows, lampshades, portable device displays, and panel screens [1–5]. Accordingly, the design and fabrication of a transparent counter electrode (CE) with a high ability for reducing I_3^- to I^- to complete the cycle of electron transport is highly demanded.

Platinum is a common active component of the CE in DSSCs because of its excellent redox activity for the I_3^-/I^- couple. Thus, transparent thin-layer Pt CEs have been fabricated through sputtering or thermal deposition [3,6]. However, the high cost, the high energy-consuming process, and the high reflectance of thin Pt films restrict the realisation of a bifacial DSSC module [7]. Accordingly, numerous functional materials, including carbon-based nanomaterials and conducting polymers, have been proposed to replace Pt as alternative materials of CEs in DSSCs. Carbon-based nanomaterials, such as carbon black [8], activated carbon [9,10], graphite [10–12], carbon nanotubes [13,14], graphene [15–17], and carbon nanotube-graphene composites [18,19], have been well studied. However, the catalytic activity of carbons for reducing I_3^- to I^- primarily derives from defects and oxygen-containing functional groups that block the electron transport on the graphene plane. Consequently, a certain thickness is required to achieve favourable electronic conductivity and acceptable catalytic activity. In other words, the photovoltaic performance of bifacial DSSCs with a carbon-based CE is generally lower than that of a device with a Pt CE [16,17]. However, conductive polymers such as poly(3,4-ethylene-dioxythiophene) [20], polyaniline (PANI) [3,21–25], polypyrrole (PPy) [26], and poly(3,3-diethyl-3,4-dihydro-2Hthieno-[3,4-b] [1,4] dioxepine) (PProDOT-ET2) [27], have also been employed as CEs in DSSCs. Amongst these conducting polymers, PANI is particularly suitable for the CE of bifacial DSSCs because of its environmental stability, simple and environmentally friendly processing [28], and complementary light absorption to N719 and N3 dyes, which maximise the use of rear illumination for DSSCs [3].

Recently, composites of PANI and carbon nanomaterials have attracted considerable attention because the introduction of nanocarbons effectively enhances the catalytic activity of PANI, resulting in the superior performance of DSSCs [29–32]. Drop-casting and Spin-coating is an easy way to fabricate transparent PANI/nanocarbon CE but this method only can be conducted in fabricating small devices, lacking practicability. To prevent the catalytic film from peeling off the substrate, several investigations involving electro- polymerisation to simultaneously deposit PANI and nanocarbons onto the substrate have been conducted [30-32]. However, no literature proposes an effective approach to fabricating a transparent PANI/nanocarbon CE, possibly due to that electropolymerisation generally produces a compact layer that depresses the penetration of electrolytes. As a result, the optimal performance was obtained at several micrometres of composites [22]. Chemical deposition using electrostatic adsorption to combine PANI and RGO or carbon nanotubes with a layer-by-layer structure has also been proposed while the low transparency, caused by the high content of nanocarbons, restricts the use of this method with bifacial DSSCs [33,34]. An interfacial polymerization has been proposed and successfully fabricated a transparent PANI/

nanocarbon film [35]. However, this method requires the use of organic solvent and rigorous parameter control for modulating thickness of films. Moreover, the thin film easily peels off from the substrate because of weak interaction between film and substrate. These reasons restrict the practicability of this method to prepare a transparent PANI/nanocarbon CE. Accordingly, preparing a transparent PANI/nanocarbon CE for bifacial DSSCs with excellent performances is a big challenge.
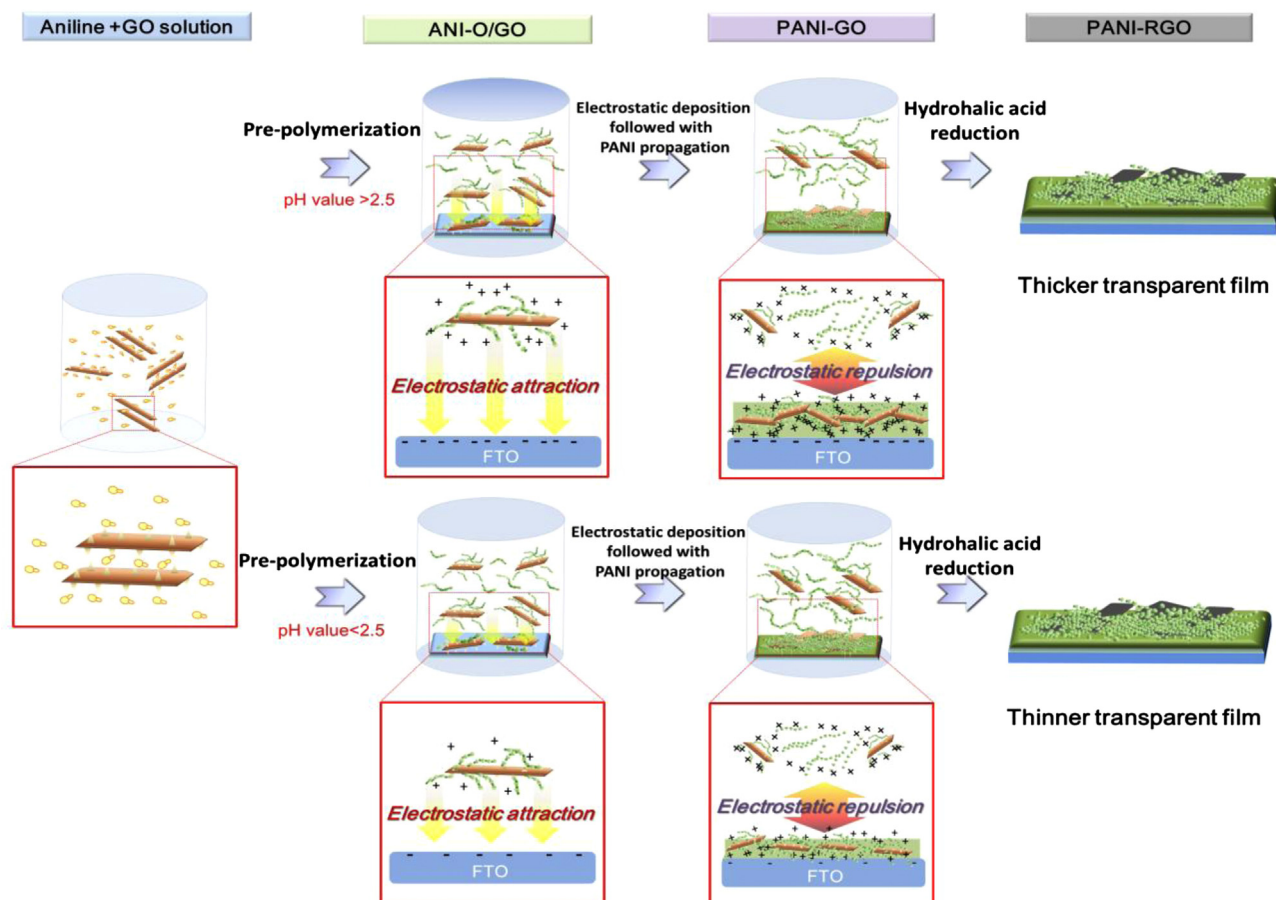
This study presents a simple, two-step approach to fabricating transparent thin films consisting of PANI and RGO using 1) an *in-situ* positive charge transformation of GO through aniline pre-polymerisation onto GO (denoted as ANI-O/GO) and electrostatic adsorption of positively charged ANI-O/GO onto fluorine-doped tin oxide (FTO), and 2) chemical reduction of PANI/GO films with hydroiodic acid (Scheme 1). In this approach, PANI not only acts as a spacer to prevent the restacking of RGO during the reduction process but also reverses the net negative charge to a positive charge around the surface of the GO during the pre-polymerisation (i.e., the ANI-O/GO formation step). The latter effect supplies an electrostatic driving force for ANI-O/GO particles to adsorb onto the negatively charged FTO surface (similar to self-assembly). Moreover, the thickness of the PANI-GO films can be self-controlled by adjusting the pH value of the precursor solution from this unique deposition mechanism. Here, the extensive oxygen groups on the well-dispersed GO in the aniline precursor solution to work as nucleation sites of the PANI propagation, leading to clear enhancement in the electrolyte-accessible area and larger short-circuit current density (J_{SC}). Furthermore, hydroiodic acid was used to prevent possible exfoliation of films caused by gas evolution when other strong reducing agents, such as sodium borohydride or hydrazine, were adopted. The RGO constructs great conductive paths within PANI, leading to faster electron transfer and larger fill factor (FF). Thus, the well-designed polyaniline-reduced graphene oxide (PANI-RGO) electrodes retained a fairly high transparency (despite contain RGO) and exhibited an excellent photovoltaic performance. Such an outstanding performance has not been achieved before because of the lack of effective transparency retention of the PANI/nanocarbon electrodes [30-32,36].

In this study, the microstructure and electrocatalytic activity of PANI-RGO and polyaniline-graphene oxide (PANI-GO) with various deposition times are examined systematically to propose the unique deposition mechanism of this novel synthesis approach. In addition, transparent bifacial DSSCs were successfully fabricated and characterised. The incorporation of RGO raised the transparency of CEs and enhanced the rear-illumination performance of DSSCs. Moreover, this transparent PANI-RGO electrode with excellent electrochemical activities is promising for other electrochemical systems, such as photo-electro-chromic devices [37], supercapacitors [38], and sensors [39], responding to the gradually increasing demand for transparent devices.

2. Experiment

2.1. Preparation of graphene oxide (GO)

Graphene oxide was prepared from raw graphite powders by a modified Hummers' method according to our previous study [40]. In a typical process, 0.25 g graphite, 0.125 g NaNO$_3$, 12 ml H$_2$SO$_4$ (98%), and 0.75 g KMnO$_4$ were added into a flask with continuous stirring for about 15 min in an ice bath. Then, this solution was ultrasonically aged in an ice bath for 3 h (Delta, 40 kHz and 200 W). Subsequently, 12 ml deionized (DI) water was added slowly into the above solution which was continuously stirred for 12 h. Finally, hydrogen peroxide was added to react with the residual permanganate and manganese dioxide. Rinsing with DI water,

Scheme 1. The route for fabricating transparent PANI-RGO composite electrodes. Step 1: aniline pre-polymerization on GO and charge transformation of GO. Step 2: electrostatic adsorption of ANI-O/GO and following polymerization of aniline. The final step employs the hydroiodic acid reduction to obtain PANI-RGO films.

centrifugation, and filtration were adopted to remove the remaining salt impurities.

2.2. Preparation of PANI, PANI-GO and PANI-RGO electrode

PANI and PANI-GO electrodes were prepared according to the rapid mixing method. For the PANI-GO electrode, two solutions (A and B) were prepared independently. Solution A was a 10-ml HCl solution containing 0.5 M aniline with different amounts of GO (0.5, 1, 1.5, and 2 wt%). Solution B was another 10-ml HCl solution containing 0.12 M potassium persulfate (KPS). pH of both solutions was adjusted to be 2.5 in order to obtain PANI-GO with good conductivity [41] and the negatively charged surface of FTO [42]. Solution B was added quickly to solution A, followed with 2 min ultrasonication at 4 °C for pre-polymerization. After the 2-min pre-polymerization for forming aniline oligomers onto GO (ANI-O/GO), a piece of well-cleaned FTO glass (TEC-7, Hartford Glass Co., USA) was immersed in the mixture and the vial was kept at 4 °C for 15 min, 1 h, and 24 h, which were labelled as PANI-GO-15 m, PANI-GO-1 h, and PANI-GO-24 h, respectively. Finally, the PANI-GO electrodes were rinsed with DI water, and then the PANI-GO layer on the nonconductive side was removed. The PANI electrode was prepared through a similar procedure for preparing PANI-GO while the only difference was the absence of GO in solution A. To obtain the PANI-RGO electrode, the PANI-GO electrodes were kept in a vial containing 55% hydroiodic acid at 90 °C for 5 min. Then, the resultant PANI-RGO electrodes were rinsed with DI water and labelled as PANI-RGO-15 m, PANI-RGO-1 h, PANI-RGO-24 h derived from PANI-

GO-15 m, PANI-GO-1 h, PANI-GO-24 h, respectively. All electrodes were stored in a vacuum reservoir and re-doped in 1 M HCl for 4 h before all electrochemical examinations.

2.3. Assemble DSSCs

For the preparation of DSSC photoanodes, the FTO glass plates were immersed into a 40 mM aqueous $TiCl_4$ solution at 70 °C for 30 min and washed with water and ethanol. TiO_2 paste (Eversolar® P-200, Everlight Chemical Co., Taiwan) was coated onto this pre-treated FTO glass by the screen printing method. The coated electrodes were heated in an air atmosphere at 325 °C for 5 min, at 375 °C for 5 min, and at 450 °C for 15 min, and finally, at 500 °C for 15 min. The thickness and photoactive area of the TiO_2 film were approximately 10 µm and 0.16 cm^2, respectively. Finally, this semi-transparent TiO_2 photoanode was once again treated with 40 mM $TiCl_4$ solution, then rinsed with water and ethanol and sintered at 500 °C for 30 min. Prior to the assembly of DSSCs, the electrodes were soaked at 40 °C for 4 h in an acetonitrile/t-butyl alcohol (volume ratio = 1) solution containing 3×10^{-4} M ruthenium dye (N719, Solaronix SA, Switzerland) to form the sensitized photoanode. The transparent platinum CE with 80% transparency was obtained by thermal deposition [6] and PANI-based CEs were prepared as described before. A 25-µm Surlyn film (SX1170-60, Solaronix SA, Switzerland) was used to separate the photoanode and the counter electrode and to seal the cell after the electrolyte was added. The electrolyte employed was a solution containing 0.6 M BMII, 0.03 M I_2, 0.10 M guanidinium thiocyanate and 0.5 M 4-

tertbutyl pyridine in a mixture of acetonitrile and valeronitrile (volume ratio, 85:15).

2.4. Material characterization and instruments

The zeta potential (ξ) of precursor solutions was measured using a Malvern Zeta Sizer Nano Series instrument, which was estimated from the electrophoretic mobility (μ) according to the Smouchowsky equation:

$$\xi = \frac{\eta\mu}{\varepsilon}$$

where η is the solution viscosity and ε is the dielectric constant of the liquid. Glancing incident angle x-ray diffraction (GIDXRD) was measured using a Rigaku TTRA III diffractometer (Japan). X-ray photoelectron spectra (XPS) were measured using a VG Scientific ESCALAB 220 iXL spectrometer with an Al Kα ($h\nu = 1486.69$ eV) X-ray source. Transmission electron microscopic (TEM) analyses were conducted on a Philips Tecnai F20 G2 electron microscope at 200 kV. Samples for the TEM examination were prepared by dropping the well-dispersed solutions on Cu grids followed by solvent evaporation in air at room temperature. The surface morphologies and cross-section of PANI, PANI-RGO-15 m, PANI-RGO-1 h and PANI-RGO-24 h were investigated by a field emission-scanning electron microscope (FE-SEM, Hitachi S-4700 I, Japan). The topography of PANI and PANI-RGO-15 m electrodes was identified by an atomic force microscope (AFM, Digital Instrument D3100).

2.5. Electrochemical characterization

Cyclic voltammetry (CV) was conducted by an electrochemical analyzer system, CHI 633C (CH Instruments, USA). The CV analysis was carried out in a three-compartment cell at 5 mV s^{-1}. An Ag/Ag$^+$ electrode (Argenthal, 799 mV vs. standard hydrogen electrode at 25 °C) was used as the reference electrode, and a platinum wire with an exposed area equal to 4 cm^2 was employed as the counter electrode. A Luggin capillary, whose tip was set at a distance of 2 mm from the surface of the working electrode, was used to minimize errors due to the IR drop in the electrolytes. The 3-MPN electrolyte for the CV, $J-V$, and EIS tests contained 50 mM lithium iodide (LiI, Acros), 10 mM I$_2$, and 500 mM lithium perchlorate (LiClO4, Acros). Photocurrent-voltage (J-V) curves were measured with a computer-controlled digital source meter (Keithley 2400) under AM 1.5, 1 sun illumination (YAMASHITA DENSO YSS-150A. Class A). The electrochemical impedance spectrum (EIS) analyzer, IM6 with Thales software (ZAHNER, Germany), was employed to measure and analyze the EIS spectra. The potential amplitude of ac was equal to 10 mV meanwhile the frequency range was from 100 kHz to 100 mHz. All reagents not otherwise specified in this work were Merck, GR.

3. Results and discussion

3.1. Charge transformation of GO through aniline pre-polymerisation

In this study, aniline monomers were polymerised and expected to anchor onto the surface of graphene oxide (GO) to form ANI-O/GO particles in the precursor mixture. The successful anchoring of aniline oligomers onto GO was confirmed by performing a zeta potential measurement. Fig. S1 shows photographs of the mixed solutions containing GO, aniline/GO, and ANI-O/GO dispersed in deionised water. In general, a solution with a larger deviation in the

zeta potential from 0 exhibits a greater dispersion property and a smaller particle size. GO exhibited great dispersion in the aqueous phase because of its high content of negatively charged oxygen-functional groups. However, clear aggregation and precipitation were observed for the solution containing aniline and GO. The addition of aniline changed the zeta potential of the solution from −24.5 to +3 mV, which suggests the formation of micelles, in which the N−H group of aniline monomers interacted with the oxygen-functional groups to form hydrogen bonding and exposed the benzene segment to the water molecules. This interaction hindered the negative charge around GO and caused the zeta potential to approach 0. However, the aggregation disappeared after the aniline monomers were polymerised. This phenomenon could reasonably be attributed to the positive charge of PANI chains caused by proton doping, which caused the aniline monomers to attach to the negatively charged GO and increased the zeta potential from +3 to +45.5 mV. Again, this highly positive charge deviation from 0 facilitated the dispersion of the ANI-O/GO particles in the aqueous solution. Thus, even after 1 h of standing, no precipitation appeared at the bottom of the vial. This result suggests strong interactions between the PANI chains and GO, which changed the zeta potential of the ANI-O/GO particles, and cannot simply be considered an intercalation of the PANI chains between the GO layers.

3.2. Characterization of PANI, PANI-GO and PANI-RGO composite films

Because of the electrostatic attraction forces (see Scheme 1), the positively charged ANI-O/GO particles spontaneously anchored onto the negatively charged FTO. Subsequently, the chemical polymerisation of aniline occurred on the FTO surface to form a thin film (denoted as PANI-GO). Here, GIDXRD (Fig. S2), and XPS (Figs. S3 and S4), were used to confirm the successful formation of a PANI-GO thin film on the FTO surface. Fig. S2 shows the GIDXRD patterns of the PANI, PANI-GO, and PANI-RGO films on FTO. The inset shows the diffraction pattern of the stacked GO, where a strong peak appears at $2\theta = 11.3°$, corresponding to the (002) facet with the layer spacing of GO equal to 7.79 Å. For PANI, the pattern exhibited three characteristic peaks centred at $2\theta = 14.2°$, $19.95°$, and $25.15°$, corresponding to the crystalline phase of PANI [43]. In comparison with PANI, the patterns of PANI-GO and PANI-RGO show an additional peak at $2\theta = 5°-10°$, which corresponds to the (002) facet of GO. The diffraction peak corresponding to the GO (002) facet shifted to a smaller angle and became broader than the stacked GO, because the PANI chains that attached to the GO enlarged the distance between the GO sheets. Therefore, GO can be considered to be dispersed within the PANI matrix. This effect disrupts the ordered stacking of dried GO [44]. After the film was reduced with hydroiodic acid, the diffraction peak corresponding to the (002) facet slightly shifted to a higher angle, possibly because of the removal of oxygen-containing functional groups and the transformation of chain conformation between the RGO sheets during the reduction.

Fig. S3 shows the XPS C 1s core-level spectra of PANI, PANI-GO, and PANI-RGO on the FTO and GO powders. Fig. S3a shows the typical asymmetrical characteristics of the C 1s spectrum for PANI, which can be decomposed into four Gaussian−Lorentzian peaks, centred at 284.7 (C−C or C−H), 285.9 (C−N, C=N), 286.6 (C−N$^+$ or C−O), and 287.9 eV (C=O) [45,46]. Comparing with Fig. S3a for PANI, an additional shoulder appears between 286 and 290 eV for the spectrum of PANI-GO (see Fig. S3b), which is attributed to the presence of C=O, C−O, and O−C=O groups on GO [47]. After this film was reduced with hydroiodic acid, the oxygen-containing functional groups were removed nearly completely and only a

few C=O groups originating from PANI were visible on the PANI-RGO film (Fig. S3c). Accordingly, the XPS C 1s spectra of PANI and PANI-RGO were similar. In Fig. S3d, two well-separated peaks are visible. This phenomenon is attributable to the absence of the C–N or C=N species. Based on the aforementioned analyses and discussion of the zeta potential, dispersion ability, GIDXRD patterns, and XPS spectra, PANI-GO can be spontaneously deposited onto FTO through an electrostatic deposition mechanism. In addition, hydroiodic acid is an effective agent for reducing GO within the PANI-GO film (see Table 1).

Fig. S4 shows the XPS N 1s core-level spectra of the PANI, PANI-GO, and PANI-RGO thin films on FTO. According to the Gaussian–Lorentzian fitting, these N 1s spectra can be reasonably decomposed into three constituents for the quinonoid imine (−N=, 398.7 eV), benzenoid amine (−NH−, 399.8 eV), and positively charged nitrogen (N+, 401.6 eV), which correspond to the three major types of nitrogen bonding on the PANI backbone [45,46]. The relative ratios of the three nitrogen species for PANI, PANI-GO, and PANI-RGO were obtained from the relative area below the constituent peaks, as shown in Table 2. PANI-GO exhibited a lower ratio of quinonoid imine and a higher amount of positively charged nitrogen than PANI did, because GO doping occurred on the quinoid segment of PANI, which induced the quinonoid imine in the doped state (i.e., the positively charged nitrogen) [46]. After hydroiodic acid reduction, a substantial amount of quinonoid imines were reduced to benzenoid amines, but the positively charged nitrogen atoms that dominated the conductivity of PANI did not decrease significantly. This result indicates that GO doping might restrain the reduction of positively charged nitrogen into benzenoid amine, causing a non-significant decrease of conductivity for PANI during the reduction process.

3.3. Effects of varying the GO/aniline ratio

To investigate effects of varying the GO/aniline ratio in the deposition system developed in this work, the PANI-RGO-15 m were prepared when the aniline solutions include 0.5, 1, 1.5, and 2 wt% GO and the corresponding CV curves of I_3^-/I^- on these electrodes were shown in Fig. S5. Note the obvious aggregation last during the deposition process when the GO concentration exceeds 2 wt%, which leads GO to become too heavy to be pulled onto FTO by the electrostatic force. Consequently, the GIDXRD pattern of PANI-RGO shows no RGO signal when the GO concentration exceeds 2 wt%. Fig. 1 shows the peak separation and cathodic peak current density of I_3^-/I^- for PANI CE and PANI-RGO-15 m CEs with the aniline solutions containing 0.5, 1, 1.5, and 2 wt% GO. An obvious decrease in the peak separation and an increase in the peak current density can be observed when aniline solution contains GO, revealing that GO incorporation enhances the electrocatalytic activity of PANI for the I_3^- reduction because of the great synergistic effect between RGO and PANI. This enhancement becomes stronger along with a larger GO wt% in the aniline solution while it maintains constant when the GO content in the aniline solutions exceeds 1 wt%. This phenomenon implies that the RGO amount incorporated into PANI-RGO possibly achieves saturation at 1 wt% of GO and the excess GO may be not pulled onto FTO by the electrostatic

Table 1
The zeta potential of GO, ANI/GO and ANI-O/GO dispersed in HCl solution at pH = 2.5

Sample	Zeta potential
GO	−24.5 mV
ANI/GO	+3 mV
ANI-O/GO	+45.5 mV

Table 2
The relative ratio of three nitrogen bonding for PANI, PANI-GO and PANI-RGO.

Sample	Oxidized state, −N= (398.2 eV)	Reduced state, −NH− (398.3 eV)	Doped state, −N+− (398.2 eV)
PANI	70.20%	19.80%	9.90%
PANI-GO	37.90%	43.60%	18.50%
PANI-RGO	12.90%	70.60%	16.60%

force. Thus, the optimal amount of GO in aniline solutions is 1.0 wt% which has been employed for the following studies.

3.4. Microstructures of PANI and PANI-RGO composite films

Fig. 2 shows the SEM images of PANI, PANI-RGO-15 m, PANI-RGO-1 h, and PANI-RGO-24 h. PANI generally exhibits a homogenous morphology with numerous cauliflower-like particles that are aggregates of small granules. However, by introducing RGO, an obvious change in the morphology was observed. In Fig. 2b, the SEM images of PANI-RGO show numerous worm-like PANI clusters with a small granular morphology appearing around the RGO, whereas the region without RGO retained the original PANI morphology. This result suggested that the formation of worm-like clusters was caused by the presence of RGO.

More detailed SEM images of PANI-RGO are presented in Fig. 2c. These images reveal that nanorod arrays were vertically aligned on RGO, and some rods elongate and propagate to form the worm-like PANI granules. This phenomenon suggests that the oxygen-containing functional groups of GO provide heterogeneous nucleation sites during the pre-polymerisation period, resulting in the formation of nanorod arrays and worm-like PANI [48]. This worm-like PANI might render a porous structure and a rough surface of PANI-RGO, increasing the electrolyte-accessible area. According to a comparison of the SEM images in Fig. 2b, d and e, the electrostatic deposition of ANI-O/GO and the propagation of PANI on the well-cleaned FTO enhanced the formation of worm-like PANI when the deposition time was 1 h (see Fig. 2d), because the morphology of PANI-GO was not significantly changed by the hydroiodic acid reduction. Moreover, the smooth and compact surface of PANI-RGO-24 h indicated that the pores within the film were filled because of the over propagation of PANI (Fig. 2e).

Fig. 3 shows the cross-sectional images of PANI and various PANI-RGO films on FTO. PANI granules with a considerably rough morphology grew on the FTO surface. The PANI-RGO-15 m film exhibited a coarser structure than the PANI granules did. In addition, the granular boundary was unclear for this composite. This
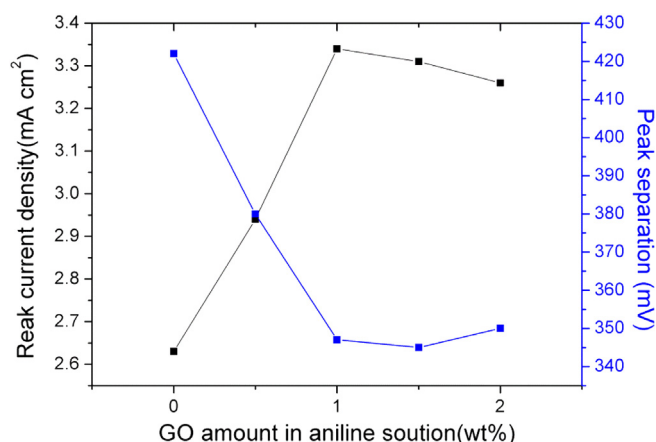

Fig. 1. The Peak separation and cathodic current density for PANI CE and PANI-RGO-15 m CEs with the aniline solutions including 0.5 wt%, 1 wt%, 1.5 wt%, and 2 wt% GO.
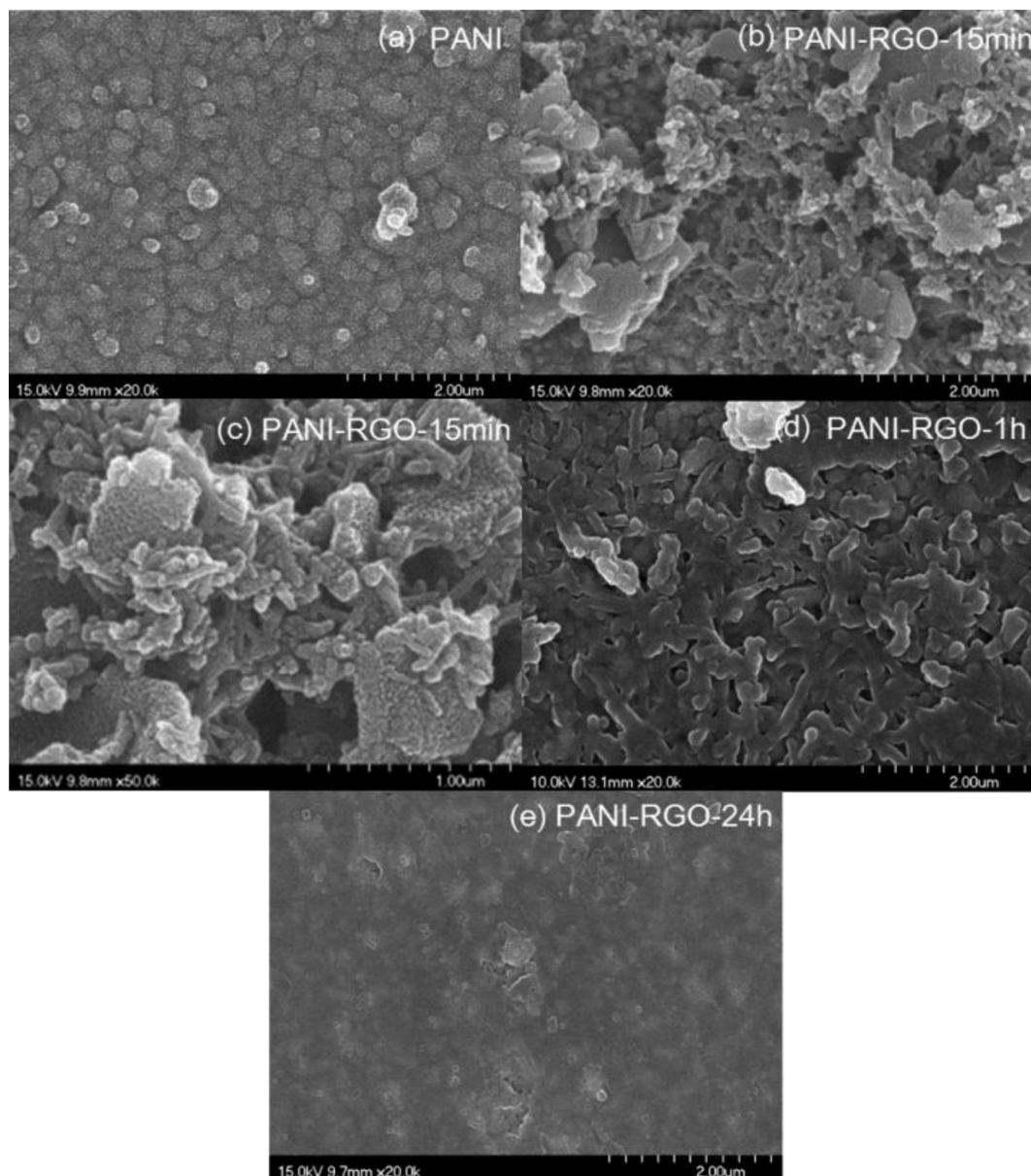
Fig. 2. SEM images of (a) PANI, (b,c) PANI-RGO-15 m, (d) PANI-RGO-1 h, and (e) PANI-RGO-24 h.

phenomenon was similar to our previous study on using the TiO_2/RGO-CNT composite as photoanodes in DSSCs [49]. Because of the high density of oxygen-containing functional groups, the aniline monomer tends towards heterogeneous nucleation on GO to form ANI-O/GO at the pre-polymerisation step. The following spontaneous deposition of positively charged ANI-O/GO onto the negatively charged FTO facilitated the propagation of PANI. In other words, GO functioned as the nucleation site to form ANI-O/GO and the *in-situ*-generated ANI-O/GO functioned as the scaffold in the composite film for PANI growth, causing the porous, coarse structure and rough surface. Prolonging the deposition time caused PANI to over-propagate and fill the pores of the composite film, because the film thickness was not significantly changed by prolonging the deposition time according to Fig. 3. Therefore, a compact film with a smooth surface was observed for PANI-RGO-24 h (see Figs. 2e and 3d).

The deposition time and RGO incorporation did not significantly change the thickness of all films on the FTO substrates,

supported by the fact that the thickness of all films was approximately 650–730 nm. Because the deposition of PANI-GO onto FTO strongly depended on the electrostatic force which is proportional to the quadratic inversion of the distance, the positively charged ANI-O/GO quickly assembled on the negatively charged FTO when the FTO was placed into vials. However, the accumulation of positively charged PANI or PANI-GO films compensated the negative charges on FTO, and thus the electrostatic attraction force became negligible at a particular thickness. Hence, during the initial immersion period, the positively charged aniline oligomers and ANI-O/GO could be effectively deposited onto FTO to form a thin film. Due to the charge compensation effect on the FTO deposited with the thin film, only aniline monomers could be continually polymerised onto the deposited film, further filling the pores. Therefore, the major parameters determining the film thickness are concluded to be the charge density of the negatively charged supports and the positively charged aniline oligomers and ANI-O/GO, which
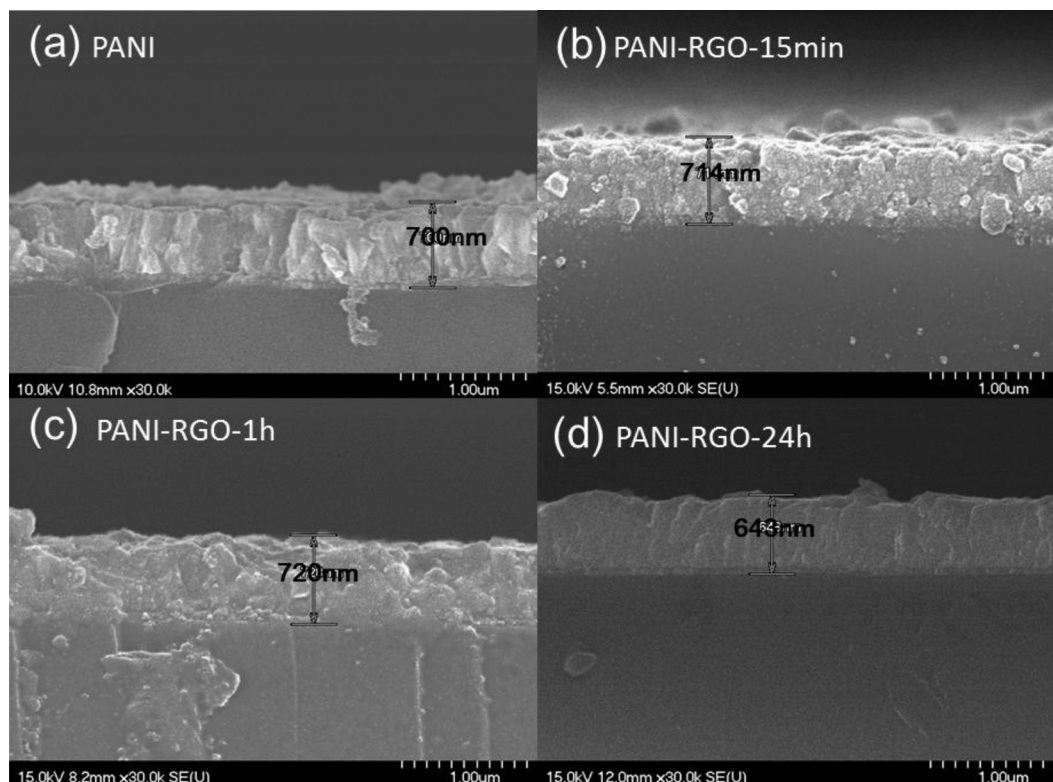
Fig. 3. The cross-section images of (a) PANI and (b—d) PANI-RGO with the deposition time equal to (b) 15 min, (c).

depends on pH of the precursor solution. Accordingly, the solution pH was varied to control the thickness of resultant films. This idea was substantiated by the results in Fig. 4, which shows the cross-sectional images of the PANI films on FTO when the pH values of the precursor solution were 2, 2.5, and 3 during the 15-min deposition. A thin layer (approximately 500 nm) was deposited onto FTO when the pH value was 2, and the thickness was approximately 700 μm when the pH values were equal to or greater than 2.5 because of the negligible variation in the zeta potential between aniline oligomers and FTO [34,42]. A thinner layer can reduce the diffusion barrier but probably exhibits a smaller electrolyte-accessible surface area. Moreover, the conductivity of PANI begins to decrease at pH greater than 3 [50]. These effects simultaneously determine the redox performance of the PANI-RGO films. Consequently, pH = 2.5 is the optimal condition for preparing PANI-RGO films (see Fig. S6).

Based on the aforementioned results and discussion, the film thickness of PANI and PANI-GO can be controlled by varying the electrostatic forces between electroactive materials and FTO substrates (see Scheme 1), which can be tuned by varying the pH of the

precursor solution. Furthermore, the porosity of ultrathin PANI-RGO films can be controlled by varying the deposition time. According to the aforementioned electrostatic deposition mechanism, the thin, porous, transparent PANI and PANI-RGO films can be formed on any negatively charged substrate that is easily obtained using several surface modification techniques (e.g., oxygen plasma, acid treatment, and oxidation).

AFM was used to confirm the morphology of the thin films grown on FTO. Typical images of PANI and PANI-RGO-15 m are shown in Fig. 5. As observed in Fig. 5a, the surface of PANI is generally rough and numerous cauliflower-like particles in a wide distribution are visible. A few large, umbonate, irregularly shaped particles were identified as the aggregates of small granules. After RGO was introduced, a considerably rougher surface with numerous umbos around the RGO sheets was visible in Fig. 5b. The PANI "worms" consisted of numerous small granular nanoparticles that connected with one another. The worm-like morphology with a rough surface further confirms that PANI-RGO provides a larger electrolyte-access area than does PANI with a cauliflower-like morphology.
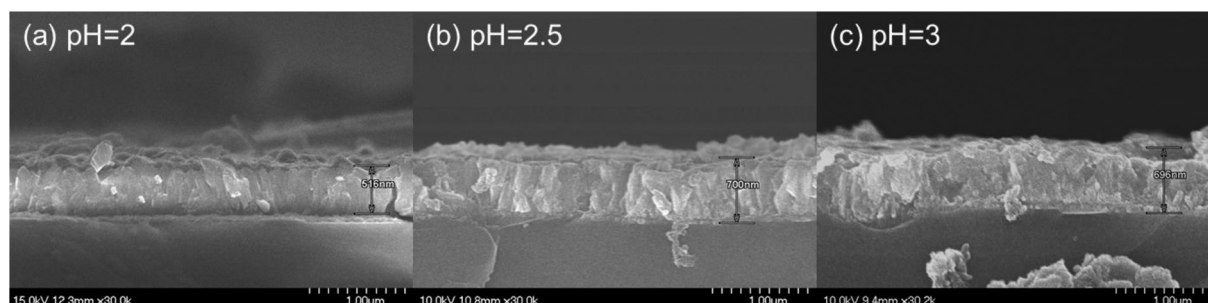

Fig. 4. The cross-section images of PANI CEs deposited at pH = (a) 2, (b) 2.5, and (c) 3. 1 h, and (d) 24 h.

Fig. 6a and b shows typical TEM images of GO and PANI-RGO-15 m resolved from the FTO substrate. The GO nanosheets without chemical reduction were observed to be flat on the copper grids because of the repulsive forces of the high-density functional groups on GO. Three-dimensional, highly porous PANI networks were deposited onto the RGO surface, as observed in Fig. 6b, confirming the heterogeneous nucleation and propagation of PANI onto GO during the immersion period of FTO. The inset in Fig. 6b shows a low-magnification TEM image of the PANI-RGO-15 m nanocomposite, revealing a flat and uniform film on the Cu grids. This result indicates that the attachment of PANI effectively inhibits the crumpling of RGO because RGO generally restacked and forms agglomerates because of the strong Van der Waal interaction between RGO nanosheets [51,52].

3.5. Electrocatalytic activity for I_3^-/I^-

CV was used to investigate the electrocatalytic activity of various counter electrodes prepared in this study towards the I_3^-/I^- couple in the 3-MPN-based electrolyte. Fig. 7 shows the typical CV curves of PANI, PANI-GO-15 m, PANI-RGO-15 m, and Pt CEs at a scan rate of 5 mV s^{-1}. All of the curves show a pair of redox peaks with a redox potential equal to approximately -0.16 V (from anodic and cathodic peak potentials), which is attributable to the redox transition of I_3^-/I^- [53]. Based on a comparison of all CV curves, several features must be emphasised. First, the Pt CE possessed the smallest peak separation among all of the CEs, which may be due to its high intrinsic electrocatalytic activity and superior electronic conductivity [3,21–24]. However, a higher peak current density of PANI indicated a higher apparent activity in comparison with Pt, which could be attributed to its high electrolyte-accessible surface area because of the porous microstructure [3,21–24]. Second, the PANI-based CEs were ranked in the following order according to the increase in peak separation: PANI-RGO-15 m (347 mV) < PANI (422 mV) < PANI-GO-15 m (800 mV). The smaller peak separation implies less polarization, which can be reasonably associated with a higher exchange current density and greater reversibility (i.e., faster electron-transfer kinetics) [16,54,55]. Because no obvious variation in the surface morphology of PANI-GO and PANI-RGO was observed in the SEM and AFM images, the enhanced electron-transfer rate of PANI-RGO can be attributed to the improved electronic conductivity of RGO reduced from GO by hydroiodic acid. Third, the PANI-based CEs were ranked in the following order

according to the decrease in peak current density: PANI-RGO-15 m (3.34 mA cm^{-2}) > PANI (2.63 mA cm^{-2}) > PANI-GO-15 m (2.37 mA cm^{-2}). This result can be attributed to (1) the higher electronic conductivity of the PANI-RGO CE and (2) the removal of negatively charged oxygen-containing functional groups from GO. The second effect indicates that the PANI-RGO film was more positively charged than PANI-GO, which emphasises the crucial influence of the electrostatic interactions between the CEs and I_3^-/I^- redox couple on the redox transition rate. Consequently, because of the synergistic effect of its higher electronic conductivity, higher electrolyte-access surface area, and similar positive charges, PANI-RGO possesses a higher apparent activity and a faster electron-transfer rate than PANI does.

3.6. Photovoltaic performances of DSSCs assembled using various CEs

Fig. 8a shows the J–V characteristics of the DSSCs assembled using PANI CEs and various PANI-RGO CEs under 1-sun illumination (AM 1.5, 100 mW cm^{-2}). The DSSC assembled with PANI-RGO-15 m exhibits a higher short-circuit current density (J_{SC}) than those assembled with PANI, PANI-RGO-1 h, and PANI-RGO-24 h. The higher J_{SC} was consistent with the coarser structure and rougher surface of PANI-RGO-15 m than that of PANI, PANI-RGO-1 h, and PANI-RGO-24 h, examined using AFM and SEM (see also Table 3) [24,56]. The FF is inversely proportional to the J_{SC} because a higher current passed through the device and a greater voltage drop was obtained according to the ohmic law [17]. Moreover, the diffusion resistance associated with the porosity may reduce the FF value, whereas the PANI-RGO-15 m with the roughest surface and the coarsest structure exhibits the most superior power conversion efficiencies (η'), likely due to the significant enhancement of the J_{SC}.

Fig. 8b shows typical J–V characteristics of the DSSCs assembled using the Pt, PANI, PANI-GO-15 m, and PANI-RGO-15 m CEs. It shows that DSSCs assembled with various PANI-based CEs possess different J_{SC} even though the amount of dye coating is the same, which reveals the cathodic reaction is a limit step in photovoltaic process [22,31,36,57] and some un-absorbed light go through the CE directly [57]. The PANI-based CEs were ranked in the following order according to the decrease in the J_{SC}: PANI-RGO-15 m > PANI > PANI-GO-15 m (see Table 3), which was consistent with the apparent activity according to the cathodic peak current density measured from the CVs. Because of the large electrolyte-
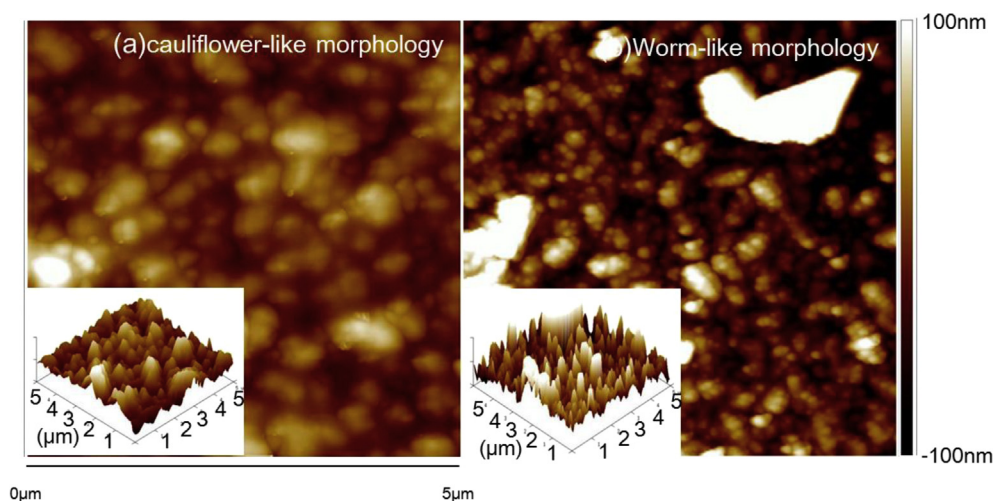

Fig. 5. AFM images of (a) PANI and (b) PANI-RGO-15 m; insets show the corresponding 3-D images.
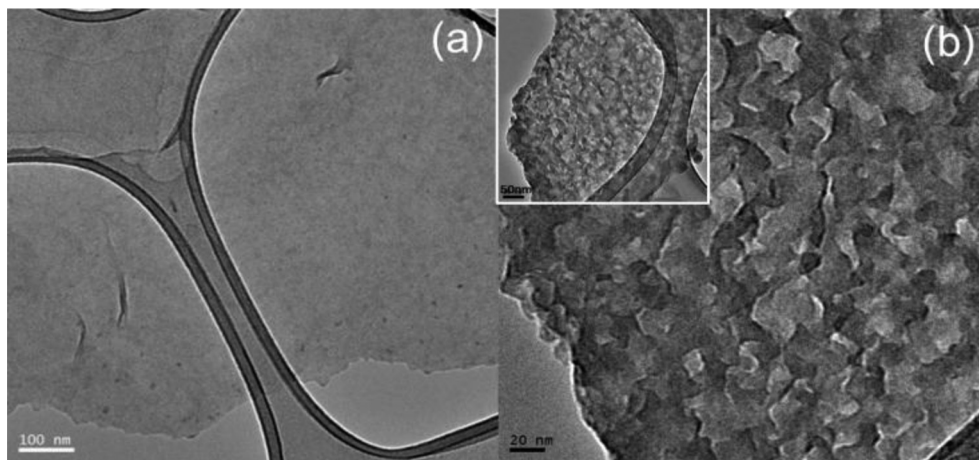
Fig. 6. TEM images of (a) GO and (b) PANI-RGO-15 m; inset in (b) shows the corresponding TEM image under a low magnification.

accessible surface area, satisfactory electron conductivity, and positively charged state, high J_{SC} values were obtained for both PANI and PANI-RGO. Accordingly, in comparison with PANI and PANI-RGO, a PANI-GO film with a large electrolyte-accessible surface area but substantially low conductivity and weak positive charge density slightly reduces the J_{SC}. Moreover, the FF obviously increases from 0.58 to 0.64 after incorporating RGO into PANI, attributable to the better electron conductivity of PANI-RGO than that of PANI. Consequently, the DSSC with a PANI-RGO-15 m CE provides a J_{SC} of 15.8 mA cm^{-2}, an open circuit voltage (V_{OC}) of 775 mV, and an FF of 0.64. The η' of this device is 7.84%, which is higher than the value obtained when the counter electrode is a PANI CE (6.7%).

Fig. 8c shows Nyquist plots of the symmetrical cells consisting of Pt, PANI, PANI-GO-15 m, and PANI-RGO-15 m electrodes, and the inset shows the equivalent circuit used to fit the EIS spectra. The ohmic series resistance (R_s) in the equivalent circuit was determined directly from the onset of the first semicircle (at the high-frequency end), which is shown in Table 3. The order of PANI-based CEs with respect to increasing R_s is: PANI-RGO (0.71 Ω cm^2) < PANI (0.78 Ω cm^2) < PANI-GO (1.69 Ω cm^2), which is in a strong agreement with the results obtained from the CV analysis. This result further supports the proposal that the electron-conductive paths have been successfully constructed within the PANI-RGO composite film. The semicircles in the high-frequency and low-frequency regions are attributed to the charge-transfer resistance (R_{CT}) and the diffusion impedance of the I_3^-/I^- couple in the electrolyte, respectively [17]. The charge transfer resistance of the I_3^-/I^- couple at the electrode/electrolyte interface were obtained by fitting the impedance data with the equivalent circuit shown in the inset (see Table 3), which can be expressed as the following equation according to the Bulter–Volmer equation [17,55]:

$$J_0 = \frac{RT}{nFR_{CT}}$$

where R_{CT} is inversely proportional to the exchange current density (J_0). According to the CV results, the order of CEs with respect to decreasing J_0 is: Pt (18.616 mA cm^{-2}) > PANI-RGO (18.081 mA cm^{-2}) > PANI (16.408 mA cm^{-2}) > PANI-GO (7.585 mA cm^{-2}), which is consistent with the prediction from the Bulter–Volmer equation. The R_{CT} values of all of the PANI-based CEs are higher than that of the Pt CE because of the lower intrinsic electrocatalytic activity/conductivity of PANI [3]. Fortunately, J_{SC} of

the DSSCs assembled with the PANI-RGO CEs is still comparable with that assembled with Pt, which may be attributed to their higher electrolyte-accessible surface area [3]. The DSSC assembled with the PANI-GO-15 m CE exhibits the highest R_{CT} among all DSSCs with the PANI-based CEs because of its worse electron conductivity and a less positively charged state, resulting in the lowest FF. Again, because of the synergistic effect of high electronic conductivity, high electrolyte-access surface area, and similar positive charge state, the DSSC assembled with the PANI-RGO-15 m CE possesses a lower R_{CT} value than that assembled with the PANI CE. This effect reduces the polarization of I_3^- reduction to I^- and maintains a high FF value for photovoltaic conversion [17,55]. Therefore, although a higher current density has been passed through the device, the DSSC assembled with the PANI-RGO CE possessed a higher FF value than that assembled with a PANI CE.

The performance of the DSSCs with PANI and PANI-RGO CEs under rear illumination was evaluated to produce a bifacial DSSC. The transparency and UV–Vis spectra are shown in Fig. 9 meanwhile the J–V characteristics and monochromatic incident photon-to-electron conversion efficiency (IPCE) of DSSCs in both front and rear illumination modes at the same test environment are shown in Fig. 10. From Fig. 9a, clear variations in the transparency among the PANI, PANI-GO-15 m, and PANI-RGO-15 m CEs
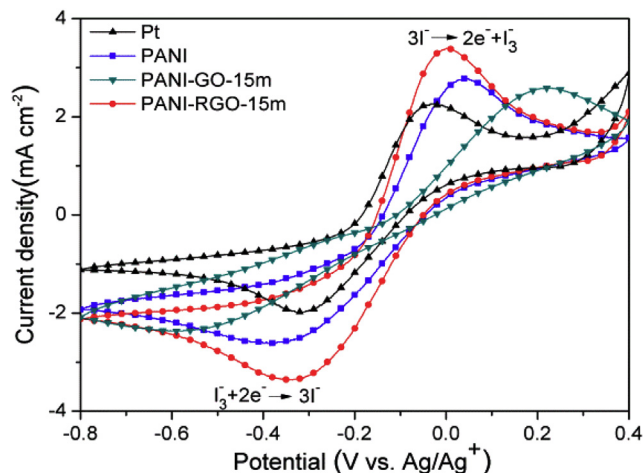

Fig. 7. Cyclic voltammograms of Pt, PANI, PANI-GO-15 m and PANI-RGO-15 m at 5 mV s^{-1} in 3-MPN containing 50 mM LiI, 10 mM I2, 500 mM LiClO4.
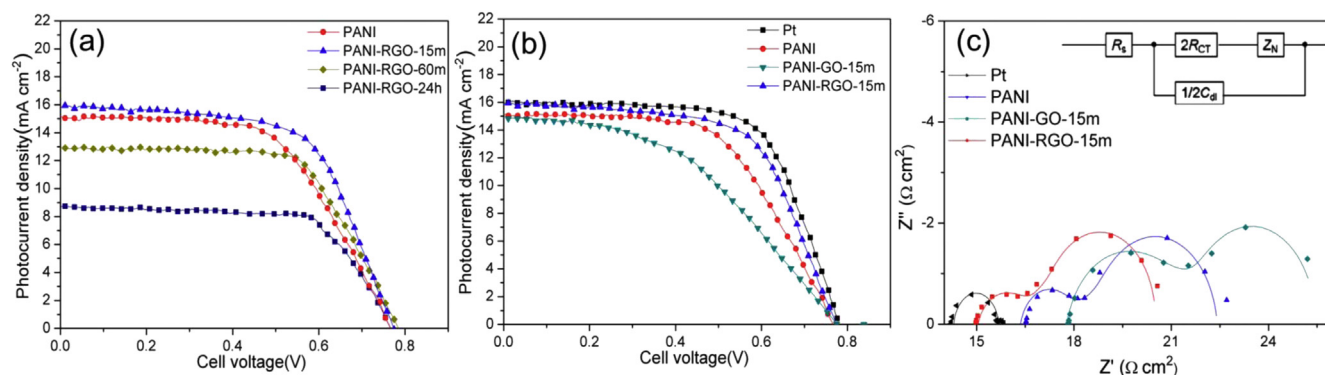
Fig. 8. (a) The photocurrent–voltage curves of DSSCs employed PANI-RGO-15 m, PANI-RGO-1 h, and PANI-RGO-24 h CEs. (b) The photocurrent–voltage curves of DSSCs employed Pt, PANI, PANI-GO-15 m, and PANI-RGO-15 m CEs. (c) The Nyquist plots of symmetric cells consisting of Pt, PANI, PANI-GO-15 m and PANI-RGO-15 m.

are observed. This phenomenon is attributable to the distributions of amine ($-NH-$) and imine ($-N=$ and $-N^+-$) since PANI of a high amine/imine ratio tends to achieve a transparent pernigraniline (PB) state and PANI of a low amine/imine ratio is close to a blue leucoemeraldine (LB) state [58,59] meanwhile the thicknesses of PANI, PANI-GO, and PANI-RGO are approximately same. Interestingly, as shown in Fig. 9b, the addition of GO significantly promotes the transmittance of PANI from a comparison of the spectra corresponding to PANI and PANI-GO. Moreover, reducing GO with hydroiodic acid effectively enhances the transmittance of PANI-RGO in the entire wavelength region of investigation in this study. All the above results are possibly due to a higher amine/imine ratio of PANI-RGO than that of PANI-GO and PANI [58,59]. Fig. 10a presents a comparison of the J–V characteristics of the DSSCs with the Pt, PANI, and PANI-RGO-15 m CEs under front- and rear-illumination modes. The J_{SC} values obtained under the front-illumination mode were consistently higher than those obtained under the rear-illumination mode because the photons from 300 to 500 nm were significantly absorbed by the catalytic layer on the CE and the electrolyte under the rear-illumination mode. Such an effect reduces the light intensity for dye absorption in comparing with the front-illumination case. Because the main absorption region of N719 dye is between 450 and 650 nm, the higher transparency and weaker absorption from 500 to 650 nm for PANI-RGO allow the dye to harvest more photons from the rear side [3]. Therefore, the DSSC assembled with the PANI-RGO CE exhibits higher retention of J_{SC} (75.5%) than does that assembled with a PANI CE (56.9%), causing an increase in the conversion efficiency retention from 69.1% to 77.6%. The efficiency retention of this device is also higher than that of the DSSC assembled with a transparent Pt CE (74.5%). The above results are also supported by

the IPCE results (see Fig. 10b). Clearly, a large part rear-light located at 300–500 nm has been absorbed by the catalytic layer and electrolyte. However, because the PANI-RGO-15 m CE possesses higher transmittance from 400 to 700 nm, its IPCE and J_{SC} are higher than that of PANI and Pt under the rear-illumination. On the other hand, the η' of DSSC with PANI-RGO CE keeps 7.1–7.3% in a 1-h visible-light soaking (AM 1.5G, 100 mW cm^{-2} at 50–55 °C) when the 3-MPN-based electrolyte was employed. In contrast, the η' of DSSC with PANI CE decays quickly from 6.1% to 5.6% in a 1-h visible-light soaking, revealing the enhancement for PANI stability after introducing RGO, possible attributed to better thermal stability of PANI-RGO.

The layer-by-layer electrostatic adsorption method mentioned in the Introduction section actually requires numerous repeated bilayer-adsorption cycles [33,34]. This complex strategy showed acceptable transmittance only when the film thickness is in the 100-nm range because every thin bilayer prepared in every adsorption cycle contains a high content of carbon nanomaterials. In comparison with such a layer-by-layer electrostatic adsorption mechanism, our newly developed method can be used to circumvent time-consuming and complex adsorption steps but maintain high transmittance under the micrometre-scale thickness. This reveals the promising application potential of the PANI-RGO CE in the bifacial DSSCs since the micrometre-scale PANI-based layers possess more catalytic sites for the I_3^- reduction.

4. Conclusions

This study demonstrates a novel two-step approach to fabricate a porous, transparent PANI-RGO counter electrode with self-controllable thickness, which is suitable for large-area production. The formation of positively charged ANI-O/GO through the pre-polymerisation step enables the deposition of PANI-GO to be an ultrathin film on FTO according to the electrostatic adsorption/deposition mechanism. This step also introduces a low GO content into the PANI-RGO film compared with the layer-by-layer electrostatic adsorption mechanism reported in previous studies [32,33]. The sequential propagation of PANI and hydroiodic acid reduction steps fabricate a uniform, transparent PANI-RGO film. Introducing RGO produces a composite film with a rougher worm-like surface and a coarser microstructure compared with that of a PANI film. The synergistic effect of enhanced electronic conductivity, higher electrolyte-access surface area, and a similar positive charge property, the DSSC with the PANI-RGO-15 m CE possesses a smaller R_{CT}, higher J_{SC}, and higher PCE than that with a PANI CE. Furthermore, the incorporation of RGO raises the amine/imine ratio as well as the transmittance of PANI,

Table 3
EIS of symmetric cells and photovoltaic characteristics of DSSCs with Pt, PANI, PANI-GO-15 m and PANI-RGO15 m CE.

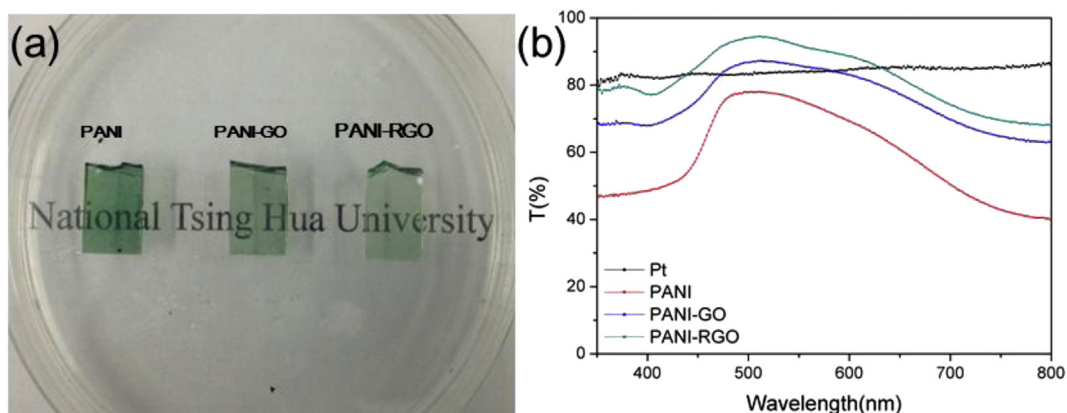|	J_{SC} (mA cm^{-2})	V_{OC} (V)	FF	Efficiency (%)	R_{CT} (Ω cm^2)
Pt (TiO$_2$ without scatter layer)	15.9	0.780	0.66	8.19	0.69
PANI	15.13	0.764	0.58	6.70	0.78
PANI-GO-15 m	15.08	0.775	0.45	5.26	1.69
PANI-RGO-15 m	15.8	0.775	0.64	7.84	0.71
Rear illumination, Pt	11.32	0.764	0.72	6.1	–
Rear illumination, PANI	8.61	0.746	0.72	4.63	–
Rear illumination, PANI-RGO-15 m	11.93	0.750	0.68	6.08	–

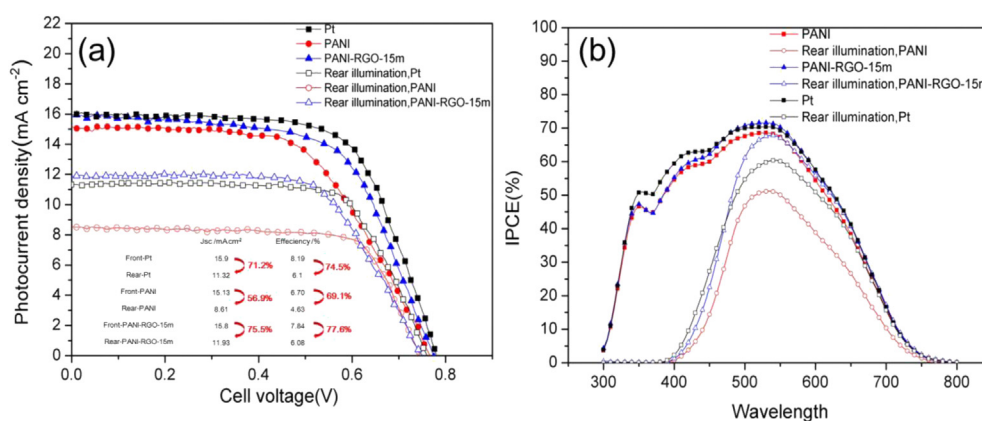**Fig. 9.** (a) The photograph and (b) UV–Vis spectra of PANI, PANI-GO and PANI-RGO electrodes.

Fig. 10. (a) The photocurrent–voltage curves of the DSSCs with PANI and PANI-RGO electrodes under the front and rear illumination modes.(b) The IPCE of DSSCs with PANI and PANI-RGO electrodes under the front and rear illumination modes.

facilitating the photo harvest from the rear side. Consequently, the device assembled with the transparent PANI-RGO CE exhibits excellent PCE retention (approximately 77.6%) between the rear- and front-illumination modes. Based on the charge transformation of GO and electrostatic deposition mechanism, the thin, porous, and transparent PANI and PANI-RGO films can be formed on any negatively charged substrate. The thickness and porosity of PANI and PANI-RGO films can be tuned by varying the pH of the precursor solution and deposition time, respectively. Therefore, the universal approach developed in this study is well suited for fabricating PANI-RGO-based/PANI-based conductive thin films.

Acknowledgements

Appendix A. Supplementary data

Supplementary data related to this article can be found at http://dx.doi.org/10.1016/j.jpowsour.2014.02.090.

References

[1] R. Hezel, Prog. Photovolt. Res. Appl. 11 (2003) 549–556.
[2] S. Ito, S.M. Zakeeruddin, P. Comte, P. Liska, D. Kuang, M. Grätzel, Nat. Photonics 2 (2008) 693–698.
[3] Q. Tai, B. Chen, F. Guo, S. Xu, H. Hu, B. Sebo, X.-Z. Zhao, ACS Nano 5 (2011) 3795–3799.
[4] B. Cosar, K.C. Icli, H.I. Yavuz, M. Ozenbas, Electrochim. Acta 87 (2013) 425–431.
[5] S.H. Park, K.-H. Shin, J.-Y. Kim, S.J. Yoo, K.J. Lee, J. Shin, J.W. Choi, J. Jang, Y.-E. Sung, J. Photochem. Photobiol. A Chem. 245 (2012) 1–8.
[6] N. Papageorgiou, W.F. Maier, M. Grätzel, J. Electrochem. Soc. 144 (1997) 876–884.
[7] G.K. Mor, K. Shankar, M. Paulose, O.K. Varghese, C.A. Grimes, Nano Lett. 6 (2005) 215–218.
[8] T.N. Murakami, S. Ito, Q. Wang, M.K. Nazeeruddin, T. Bessho, I. Cesar, P. Liska, R. Humphry-Baker, P. Comte, P. Péchy, M. Grätzel, J. Electrochem. Soc. 153 (2006) A2255–A2261.
[9] K. Imoto, K. Takahashi, T. Yamaguchi, T. Komura, J.-i. Nakamura, K. Murata, Sol. Energy Mater. Sol. Cells 79 (2003) 459–469.
[10] J. Chen, K. Li, Y. Luo, X. Guo, D. Li, M. Deng, S. Huang, Q. Meng, Carbon 47 (2009) 2704–2708.
[11] H. Wu, Z. Lv, Z. Chu, D. Wang, S. Hou, D. Zou, J. Mater. Chem. 21 (2011) 14815–14820.
[12] G. Veerappan, K. Bojan, S.-W. Rhee, ACS Appl. Mater. Interfaces 3 (2011) 857–862.
[13] R.A. Sayer, S.L. Hodson, T.S. Fisher, J. Sol. Energy Eng. 132 (2010), 021007–021008.
[14] K.S. Lee, W.J. Lee, N.-G. Park, S.O. Kim, J.H. Park, Chem. Commun. 47 (2011) 4264–4266.
[15] J.D. Roy-Mayhew, G. Boschloo, A. Hagfeldt, I.A. Aksay, ACS Appl. Mater. Interfaces 4 (2012) 2794–2800.
[16] J.D. Roy-Mayhew, D.J. Bozym, C. Punckt, I.A. Aksay, ACS Nano 4 (2010) 6203–6211.
[17] L. Kavan, J.H. Yum, M. Grätzel, ACS Nano 5 (2010) 165–172.

[18] G. Zhu, L. Pan, T. Lu, T. Xu, Z. Sun, J. Mater. Chem. 21 (2011) 14869–14875.
[19] L.-H. Chang, C.-K. Hsieh, M.-C. Hsiao, J.-C. Chiang, P.-I. Liu, K.-K. Ho, C.-C.M. Ma, M.-Y. Yen, M.-C. Tsai, C.-H. Tsai, J. Power Sources 222 (2013) 518–525.
[20] S. Ahmad, J.-H. Yum, Z. Xianxi, M. Gratzel, H.-J. Butt, M.K. Nazeeruddin, J. Mater. Chem. 20 (2010) 1654–1658.
[21] Q. Li, J. Wu, Q. Tang, Z. Lan, P. Li, J. Lin, L. Fan, Electrochem. Commun. 10 (2008) 1299–1302.
[22] J. Zhang, T. Hreid, X. Li, W. Guo, L. Wang, X. Shi, H. Su, Z. Yuan, Electrochim. Acta 55 (2010) 3664–3668.
[23] Z. Li, B. Ye, X. Hu, X. Ma, X. Zhang, Y. Deng, Electrochem. Commun. 11 (2009) 1768–1771.
[24] S. Cho, S.H. Hwang, C. Kim, J. Jang, J. Mater. Chem. 22 (2012) 12164.
[25] S. Ameen, M.S. Akhtar, Y.S. Kim, O.B. Yang, H.-S. Shin, J. Phys. Chem. C 114 (2010) 4760–4764.
[26] J. Wu, Q. Li, L. Fan, Z. Lan, P. Li, J. Lin, S. Hao, J. Power Sources 181 (2008) 172–176.
[27] K.-M. Lee, P.-Y. Chen, C.-Y. Hsu, J.-H. Huang, W.-H. Ho, H.-C. Chen, K.-C. Ho, J. Power Sources 188 (2009) 313–318.
[28] D. Li, J. Huang, R.B. Kaner, Acc. Chem. Res. 42 (2008) 135–145.
[29] H. Niu, S. Zhang, Q. Ma, S. Qin, L. Wan, J. Xu, S. Miao, RSC Adv. 3 (2013) 17228–17235.
[30] C.-Y. Liu, K.-C. Huang, P.-H. Chung, C.-C. Wang, C.-Y. Chen, R. Vittal, C.-G. Wu, W.-Y. Chiu, K.-C. Ho, J. Power Sources 217 (2012) 152–157.
[31] K.-C. Huang, J.-H. Huang, C.-H. Wu, C.-Y. Liu, H.-W. Chen, C.-W. Chu, J.-T.s. Lin, C.-L. Lin, K.-C. Ho, J. Mater. Chem. 21 (2011) 10384–10389.
[32] G. Wang, W. Xing, S. Zhuo, Electrochim. Acta 66 (2012) 151–157.
[33] K. Sheng, H. Bai, Y. Sun, C. Li, G. Shi, Polymer 52 (2011) 5567–5572.
[34] M.N. Hyder, S.W. Lee, F.Ç. Cebeci, D.J. Schmidt, Y. Shao-Horn, P.T. Hammond, ACS Nano 5 (2011) 8552–8561.
[35] S.H. Domingues, R.V. Salvatierra, M.M. Oliveira, A.J.G. Zarbin, Chem. Commun. 47 (2011) 2592–2594.
[36] G. Wang, S. Zhuo, W. Xing, Mater. Lett. 69 (2012) 27–29.
[37] K.-Y. Shen, C.-W. Hu, L.-C Chang, K.-C. Ho, Sol. Energy Mater. Sol. Cells 98 (2012) 294–299.
[38] H.-P. Cong, X.-C. Ren, P. Wang, S.-H. Yu, Energy Environ. Sci. 6 (2013) 1185–1191.
[39] X. Huang, N. Hu, R. Gao, Y. Yu, Y. Wang, Z. Yang, E. Siu-Wai Kong, H. Wei, Y. Zhang, J. Mater. Chem. 22 (2012) 22488–22495.
[40] Z. Liu, X.Y. Ling, X. Su, J.Y. Lee, L.M. Gan, J. Power Sources 149 (2005) 1–7.
[41] C. Laslau, Z.D. Zujovic, L. Zhang, G.A. Bowmaker, J. Travas-Sejdic, Chem. Mater. 21 (2009) 954–962.
[42] K. Kamada, S. Tsukahara, N. Soh, J. Mater. Chem. 20 (2010) 5646.
[43] U. Rana, S. Malik, Chem. Commun. (Camb.) 48 (2012) 10862–10864.
[44] G.-L. Chen, S.-M. Shau, T.-Y. Juang, R.-H. Lee, C.-P. Chen, S.-Y. Suen, R.-J. Jeng, Langmuir: ACS J. Surf. Colloids 27 (2011) 14563–14569.
[45] G. Wu, L. Li, J.-H. Li, B.-Q. Xu, J. Power Sources 155 (2006) 118–127.
[46] Y. Zhao, G.-S. Tang, Z.-Z. Yu, J.-S. Qi, Carbon 50 (2012) 3064–3073.
[47] S. Stankovich, D.A. Dikin, R.D. Piner, K.A. Kohlhaas, A. Kleinhammes, Y. Jia, Y. Wu, S.T. Nguyen, R.S. Ruoff, Carbon 45 (2007) 1558–1565.
[48] J. Xu, K. Wang, S.-Z. Zu, B.-H. Han, Z. Wei, ACS Nano 4 (2010) 5019–5026.
[49] M.-Y. Yen, M.-C. Hsiao, S.-H. Liao, P.-I. Liu, H.-M. Tsai, C.-C.M. Ma, N.-W. Pu, M.-D. Ger, Carbon 49 (2011) 3597–3606.
[50] J. Stejskal, I. Sapurina, M. Trchová, E.N. Konyushenko, Macromolecules 41 (2008) 3530–3536.
[51] Y. Si, E.T. Samulski, Nano Lett. 8 (2008) 1679–1682.
[52] S.-Y. Yang, K.-H. Chang, H.-W. Tien, Y.-F. Lee, S.-M. Li, Y.-S. Wang, J.-Y. Wang, C.-C.M. Ma, C.-C. Hu, J. Mater. Chem. 21 (2011) 2374–2380.
[53] J.-L. Lan, C.-C. Wan, T.-C. Wei, W.-C. Hsu, Y.-H. Chang, Prog. Photovolt. Res. Appl. 20 (2012) 44–50.
[54] M.-Y. Yen, C.-C. Teng, M.-C. Hsiao, P.-I. Liu, W.-P. Chuang, C.-C.M. Ma, C.-K. Hsieh, M.-C. Tsai, C.-H. Tsai, J. Mater. Chem. 21 (2011) 12880–12888.
[55] G. Yue, J. Wu, J.-Y. Lin, Y. Xiao, S.-Y. Tai, J. Lin, M. Huang, Z. Lan, Carbon 55 (2012) 1–9.
[56] K.-C. Huang, Y.-C. Wang, P.-Y. Chen, Y.-H. Lai, J.-H. Huang, Y.-H. Chen, R.-X. Dong, C.-W. Chu, J.-J. Lin, K.-C. Ho, J. Power Sources 203 (2012) 274–281.
[57] Y.-L. Lee, C.-L. Chen, L.-W. Chong, C.-H. Chen, Y.-F. Liu, C.-F. Chi, Electrochem. Commun. 12 (2010) 1662–1665.
[58] S. Pahal, M. Deepa, S. Bhandari, K.N. Sood, A.K. Srivastava, Sol. Energy Mater. Sol. Cells 94 (2010) 1064–1075.
[59] B.P. Jelle, G. Hagen, Sol. Energy Mater. Sol. Cells 58 (1999) 277–286.